Sensors & Actuators: A. Physical 399 (2026) 117463

Contents lists available at ScienceDirect

Sensors and Actuators: A. Physical

journal homepage: www.journals.elsevier.com/sensors-and-actuators-a-physical

Comparison of the propulsion of helical robots moving at low reynolds numbers based on hard- and soft-magnetic elements

Joost Wijnmaalen, Leon Abelmann*, Iulian Apachitei

Delft University of Technology, Delft, the Netherlands

HIGHLIGHTS

- First direct comparison of hard- and soft-magnetic microrobot propulsion.
- Hard-magnetic microrobots reach 4.5 times the speed of helices.
- Findings provide design rules balancing speed, geometry, and biocompatibility.

GRAPHICAL ABSTRACT

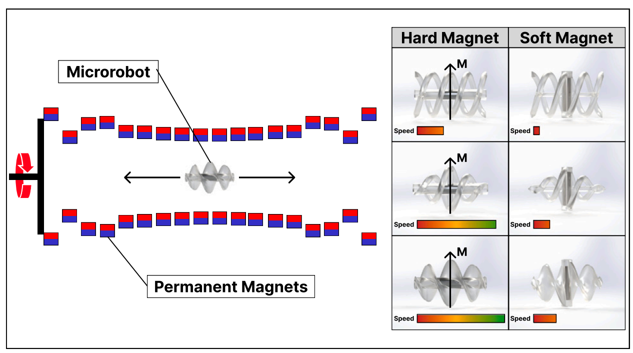

ARTICLE INFO

Keywords:
Microrobots
Biomedical
Magnetic torque
Propulsion

ABSTRACT

This study compares the propulsion of scaled-up helical microrobot models, based on hard- and soft-magnetic elements under rotating magnetic fields. The experiments were performed at the millimeter scale and interpreted using hydrodynamic scaling laws to predict microscale behavior. Results show that hard-magnetic microrobots achieved step-out frequencies and maximum propulsion speeds 4.5 times higher than soft-magnetic microrobots. Below saturation magnetization, soft-magnetic microrobots demonstrated similar performance irrespective of magnetic susceptibility, highlighting that torque generation in these materials is purely geometry-dependent. Employing a tapered ribbon design increased propulsion speed by a factor of 3.5 compared to regular helical designs. These results show that the impact of using soft rather than hard magnets is manageable, allowing for biodegradable magnets such as pure iron. The theory and experiments in this paper provide a quantitative basis for selecting materials and designs.

1. Introduction

Over the past decade, microrobots have emerged as a versatile platform for biomedical applications, including the physical removal of blood clots and biofilms [1,2], targeted drug delivery [3], and thermal ablation of bacterial infections [4].

Microrobots typically have a polymeric structure created through two-photon polymerization or micro-stereolithography [5]. The energy for self-propulsion can be extracted from the fluid (for instance H_2O_2 or glucose) [6] or from a time-varying external field (magnetic [7], acoustic [8]). Often, a external magnetic field is used to apply torque to the microrobot for steering. If the magnetic field is required anyway

* Corresponding author.
Email address: l.abelmann@tudelft.nl (L. Abelmann).

https://doi.org/10.1016/j.sna.2026.117463
Received 6 October 2025; Received in revised form 15 December 2025; Accepted 5 January 2026
Available online 5 January 2026

for steering, it may as well be used for propulsion. This enables precise microrobot control using tri-axial Helmholtz coil systems, and also allows for magnetic heating [9,10]. The magnetic component can consist of either hard- or soft-magnetic materials. Hard-magnetic materials, or permanent magnets, retain their magnetization over extended periods. They are favored for their ability to generate high magnetic torques, with NdFeB as a typical choice [11,12]. However, NdFeB exhibits cytotoxic properties, necessitating careful consideration for in vivo use, even when the microrobots are removed after use [13]. In contrast, soft magnetic materials lose their magnetic moment quickly. Typical examples like pure iron or iron-oxide are biocompatible but provide limited torque output, which might constrain their use [3,14].

Despite these trade-offs, a direct experimental comparison between hard- and soft-magnetic based microrobots has, to our knowledge, not been conducted. Such an analysis would contextualize the usability of magnetic materials already used in microrobots, such as NdFeB and iron-oxides, and validate the integration of novel materials such as biodegradable pure Fe, which could be incorporated as thin wires down to 25 μm.

In this study, we compare the propulsion of hard- and soft-magnetic microrobots under rotating magnetic fields. Microrobots for medical applications typically have dimensions below 1 mm [15] and move at speeds below ten body lengths per second [6]. Our target dimension is 0.5 mm, where the immune response is still absent. At these scales and velocities, the microrobots operate in the Stokes-flow regime, where viscous forces dominate over inertia. To study propulsion in this regime, we can increase the size of the robots while proportionally increasing the viscosity of the surrounding medium by using glycerin. This approach preserves the relevant flow physics, simplifies the experiments, and enables more precise measurements. Since we focus on the difference between microrobots with hard or soft magnets, we restricted the trajectory to a straight line by confining the microrobot in a tube, allowing for simple, precise experiments. Therefore the magnetic field configuration was optimized for propulsion only.

We studied three distinct microrobot geometries, each fabricated with three different magnetic materials: NdFeB (hard-magnetic), MnZ ferrite (soft-magnetic), and pure Fe (soft-magnetic). This resulted in nine unique microrobots, all 10 mm in length, allowing us to compare the performance of the magnetic elements as well as the geometry.

2. Theory

2.1. Magnetic torque

The helical microrobots in our study translate rotation around their long axis into forward motion. This rotation is driven by a uniform, externally applied rotating magnetic field. Torque is generated either by embedding a permanent magnet whose magnetization is perpendicular to the direction of motion, or by using a soft-magnetic cylinder oriented with its long axis perpendicular to this direction (see Fig. 2).

For hard-magnetic microrobots, magnetic torque arises from the tendency of the magnet's fixed magnetization to align with an external magnetic field. Maximum torque is achieved when the magnetization and field are perpendicular, and is given by [16]:

$$T_{\max}^{\text{hard}} = \mu_0 V M H_0 \text{ (Nm)}, \tag{1}$$

where μ_0 is the vacuum permeability (N/A^2), V the volume of the magnetic element (m^3), M the magnetization (A/m), and H_0 the applied external magnetic field strength (A/m).

In soft-magnetic microrobots, torque arises from shape anisotropy. Shape anisotropy depends on geometry, favoring alignment of the material's long axis with the external magnetic field to minimize magnetic energy. When an external magnetic field is applied at an angle to this axis, torque is generated. Maximum torque is reached when the external magnetic field is angled 45° relative to the long axis of the soft-magnetic material, and is defined by Abbott et al. [17]:

$$T_{\max}^{\text{soft}} = \frac{\mu_0 V H_0^2 (n_\text{r} - n_\text{a})}{2 n_\text{a} n_\text{r}} \text{ (N m)}. \tag{2}$$

Here, n_r and n_a represent the demagnetization factors in the radial and axial (long) directions, respectively, which can be approximated with ellipsoid demagnetization factors. This equation is valid only when the internal magnetization remains below saturation, defined as:

$$H_\text{low} = \frac{M_\text{s} n_a n_r \sqrt{2}}{\sqrt{n_a^2 + n_r^2}} \text{ (A/m)}, \tag{3}$$

where M_s is the saturation magnetization (A/m). By approximating the cylindrical magnets used in this study (aspect ratio 7.1) as ellipsoids with an identical aspect ratio, saturation fields ($\mu_0 H_\text{low}$) of 23 mT for ferrite and 86 mT for iron were calculated using Osborn's equations [18]. The magnetic field in our experiments remains below these values. The torque equations for $H_0 > H_\text{low}$ are provided in Supplementary Material 1 together with the derivations of Eqs. (1)–(3).

2.2. Microrobot hydrodynamics

The forward motion of the helical microrobots in viscous fluids (Re $\ll 1$), is related to their rotational velocity by [19]:

$$v = -\frac{b}{a}\omega \text{ (m/s)}. \tag{4}$$

Here, a represents the resistance to forward motion (N.s/m), and b denotes the coupling between rotation and translation (N.s), both dependent on microrobot geometry and fluid viscosity. The maximum forward velocity v_max is limited by the highest rotational frequency at which the microrobot can maintain synchronous rotation with the external magnetic field, known as the step-out frequency ω_max (Hz), given by:

$$\omega_\text{max} = \frac{a}{ac - b^2} T_\text{max} \text{ (Hz)}, \tag{5}$$

where c is the rotational resistance (N.s.m). Above this rotational frequency, the rotation becomes erratic, and the forward velocity drops upon further increase in the frequency. The step-out frequency provides an indirect measure of the magnetic torque on the microrobot, which cannot be easily assessed by other means.

The microrobots in this study were fabricated at a scale one to two orders of magnitude larger than those envisioned for practical biomedical applications. Despite this size difference, meaningful predictions can still be made through extrapolation. This is possible because, in the laminar flow regime – characterized by Reynolds numbers much smaller than unity – the flow profile is scale-invariant. To ensure that our millimeter-scale microrobots operated in this regime, we increased the fluid viscosity by two orders of magnitude.

To extrapolate our large-scale observations to smaller microrobots, we introduce a scaling factor $\lambda < 1$. When all linear dimensions are scaled by this factor, the overall shape of the microrobot is preserved, and the surrounding flow profile remains geometrically similar.

The drag coefficients a, b, and c decrease with size and viscosity as $\lambda\eta$, $\lambda^2\eta$, and $\lambda^3\eta$, respectively. Similarly, the magnetic torque, whether originating from a hard (Eq. 1) or soft magnet (Eq. 2), is proportional to the magnet's volume and thus scales as λ^3. Substituting these scaling relationships into Eqs. (4) and (5) yields:

$$v_\text{max} \propto \frac{\lambda}{\eta}. \tag{6}$$

This shows that the maximum speed scales linearly with the size of the microrobot and inversely with the viscosity of the surrounding fluid. For example, scaling a 10 mm robot down to 100 μmm and reducing the fluid viscosity from 1Pa.s to 5mPa.s would double v_max assuming all other parameters remain unchanged.

3. Experimental

3.1. Rotating magnetic field generation

The goal of the setup shown in Fig. 1, was to generate a uniform rotating magnetic field of 20 mT over a 120 mm region to enable microrobot propulsion. This system serves as a cost-effective alternative to traditional Helmholtz coil setups. The magnetic field was generated using two identical arrays (175 × 30 mm), each consisting of 3 rows and 18 columns of 5 × 5 × 5 mm N42 NdFeB magnets (Supermagnete, Gottmadingen, Germany). The distance between the opposing magnets was optimized using the Adam algorithm from the Optax library in Python [20], leading to a predicted variation in the component of the magnetic field perpendicular to the array of only 7 μT (0.035%) over a length of 12 cm. The resulting array was 3D printed using a Bambu Lab X1C, and the individual magnets were secured via press-fit. The field, as measured with a Lake Shore 455 DSP Gaussmeter, varied from 19.9–20.2 mT (1.5%). The variation is larger than predicted, most likely due to a combination of variations in magnet moments and positioning inaccuracies of the individual magnets [21]. To achieve this field strength and uniformity, one would need a Helmholtz coil set with coil diameters over 34 cm and over 3800 A·turns.

The magnetic arrays were rotated using a stepper motor and controlled through a touchscreen connected to an Arduino Uno. To ensure safe operation, the stepper motor was restricted to a maximum rotational frequency of 5 Hz.

3.2. Microrobot design and fabrication

One hard-magnetic microrobot, NdFeB (N42; first4magnets, Sutton-in-Ashfield, United Kingdom), and two soft-magnetic microrobots, MnZ ferrite (78 material; Fair-Rite, Wallkill, United States) and pure Fe (99.5 % purity; Goodfellow, Huntingdon, United Kingdom), were tested (Fig. 2). Two soft-magnetic microrobots were tested to assess the influence of magnetic susceptibility on torque generation. The NdFeB magnet measured 3 mm in length and 1 mm in diameter and had a remanent magnetization of 1.03 MA/m. The ferrite and pure Fe samples were 5.33 mm long and 0.75 mm in diameter to match the magnetic volume of the NdFeB magnet, with magnetic susceptibilities of 3000 and 8000, respectively. The saturation magnetization of 99.5 % pure Fe is 1.4 MA/m and 0.38 MA/m for 78 material ferrite. Three microrobot designs from the literature were tested: a double helix, a tapered double helix, and a tapered ribbon-shaped design [22]. All designs were 10 mm in length. The double helix had a constant width of 6.5 mm and a coil diameter of 0.8 mm. The tapered helix had the same length and maximum width but featured a 30° taper from both ends toward the center. The ribbon-shaped design consisted of a 0.3 mm thick twisted plate with a central width of 6.5 mm, tapered from both ends toward the center, also at a 30° angle.

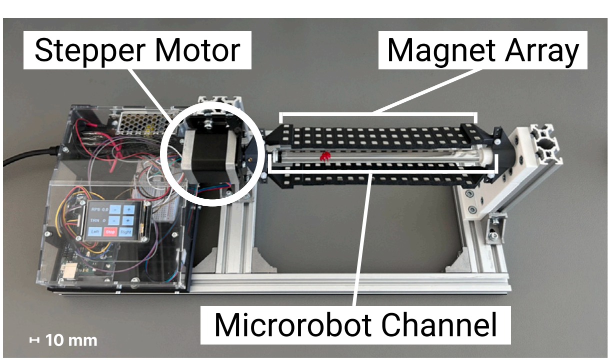

Fig. 1. Rotating magnetic field setup for generating uniform magnetic torque to propel microrobots.

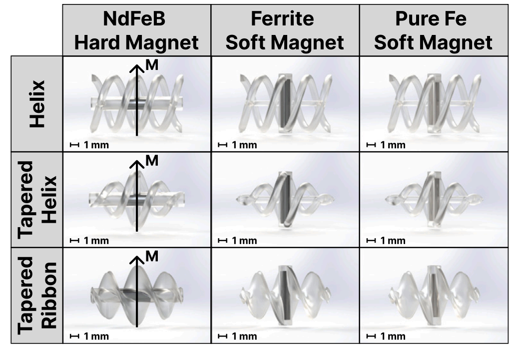

Fig. 2. Tested hard- and soft-magnetic microrobot designs, each 10 mm long, with matched magnetic volumes.

The microrobots were designed in SolidWorks (Dassault Systèmes, Vélizy-Villacoublay, France), processed using PreForm slicing software (Formlabs Inc., Somerville, MA, USA), and printed on a Formlabs Form 3 stereolithography printer (Formlabs Inc., Somerville, MA, USA) with clear V4 resin. Printed structures were washed in isopropanol (Form Wash, Formlabs; 10 min), post-cured (Form Cure, Formlabs; 30 min), and support marks were manually removed using 800-grit sandpaper. Magnetic materials were secured using UHU Magnet Glue (UHU GmbH & Co. KG, Bühl, Germany). For full fabrication details, see Supplementary Material 3.

The 3D models of all microrobot designs, corresponding PreForm files, the 3D model of the test setup, wiring diagrams, bill of materials, and optimization code are available on GitHub.

3.3. Microrobot propulsion evaluation

The microrobot was placed inside a glass tube with an inner diameter of 10 mm filled with glycerin. The microrobot was resting on the bottom of the tube. Propulsion characteristics were determined by recording the microrobot's motion over a 100 mm path at 0.1 Hz intervals using an iPhone 14 camera at 60fps (see Supplementary Material 4). The camera was placed at the center of the magnetic arrays at a distance of 120 mm. The entry and exit frames were used to determine the travel time and compute the speed. A linear fit was applied to the speed measurements up to the rotation frequency at which half the maximum speed was reached. The measurement was repeated at least three times. Subsequently, the 95 % confidence interval of the measurements was determined by:

$$\Delta v_i = 1.96\, v_i \sqrt{\left(\frac{\mathrm{RMSE}}{\bar{v}}\right)^2 + \left(\frac{\sigma_\mathrm{d}}{L}\right)^2}\ \ (\mathrm{m/s})\,, \tag{7}$$

where Δv_i is the half-width of the 95 % confidence interval for the i-th speed measurement, v_i is the corresponding speed, RMSE is the root-mean-square error of the linear fit applied to the first 50% of data points up to the maximum speed, $\bar{v}$ is the mean speed over that range, σ_d is the distance measurement uncertainty, and L is the nominal measurement length. The step-out frequency $\omega_{\max}$ was defined as the lowest rotational frequency at which three consecutive speed measurements, including their confidence intervals, fell entirely below the linear fit.

4. Results and discussion

4.1. Magnetic material comparison

Table 1 summarizes the step-out frequencies and maximum propulsion speeds for all tested materials and designs. Notably, hard-magnetic (NdFeB) microrobots achieved higher step-out frequencies and corresponding maximum speeds compared to soft-magnetic (ferrite and pure Fe) variants. Table 1 also shows that both soft-magnetic materials exhibited similar propulsion performance despite having different magnetic

Table 1
Comparison of the step-out frequency ω_{max} and the resulting maximum forward speed v_{max} with embedded hard- or soft-magnetic elements in three different microrobot designs. Microrobots based on hard-magnetic elements are 4.5 times faster than those based on soft-magnetic elements. The maximum velocity for soft-magnetic elements is independent of the material used.

Design	Magnet Type	Material	ω_{max} Hz	v_{max} mm/s
Helix	Hard	NdFeB	4.4(2)	2.7(2)
	Soft	Ferrite	1.2(1)	0.6(1)
	Soft	Pure Fe	1.1(1)	0.6(1)
Tapered Helix	Hard	NdFeB	> 5.0	> 2.8
	Soft	Ferrite	3.2(1)	1.8(1)
	Soft	Pure Fe	3.1(1)	1.8(1)
Tapered Ribbon	Hard	NdFeB	> 5.0	> 6.2
	Soft	Ferrite	2.4(1)	2.1(1)
	Soft	Pure Fe	2.3(1)	2.0(1)

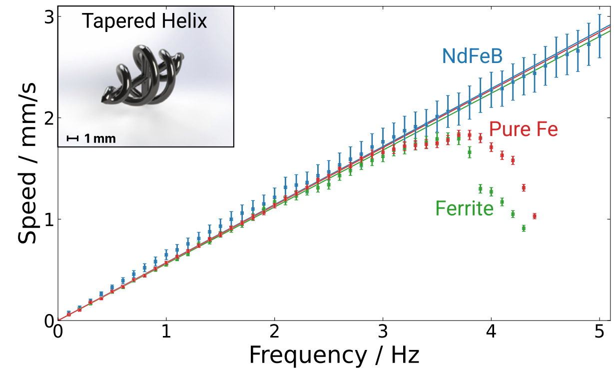

Fig. 4. Measured translation speed as a function of external magnetic field rotation frequency for one hard-magnetic (NdFeB) and two soft-magnetic (ferrite and pure Fe) tapered helical microrobots. This design achieved a threefold increase in step-out frequency and maximum speed compared to regular helical designs.

susceptibilities. This aligns with the findings of Abbott et al. [17], who reported that torque generation in soft-magnetic materials is insensitive to magnetic susceptibility. This holds true as long as the magnetic material remains unsaturated. Since commercially available Helmholtz coil systems typically operate below 20 mT, magnetic saturation is unlikely to occur when using such systems for microrobot propulsion.

4.2. Microrobot design comparison

Fig. 3 shows that hard-magnetic helical microrobots achieved a maximum speed 4.5 times higher than both soft-magnetic designs, which is close to the predicted value of 4.7 based on Eqs. (1) and (2) (see Supplementary Material 1). The nearly identical propulsion efficiencies (slope: 0.64(3)) of the hard- and soft-magnetic helical designs also indicate that the orientation of the magnetic material, whether along the length or width of the microrobot, has minimal effect on propulsion characteristics. Interestingly, the relationship between the rotational frequency of the magnetic field and translational speed became nonlinear as it approached maximum speed. This behavior contrasts with the fully linear response reported by Wang *et al.* [19]. The observed gradual loss of linearity likely results from subtle local variations in the magnetic field or from local increases in drag due to occasional wall contact. Both effects can cause the microrobot to reach the step-out frequency earlier in specific regions along its propulsion path. However, these deviations remained small, indicating minimal wall contact and underscoring the overall uniformity of the generated magnetic field.

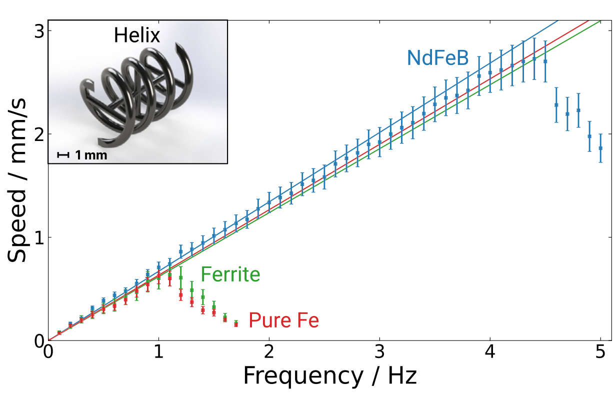

Fig. 3. Measured translation speed as a function of external magnetic field rotation frequency for one hard-magnetic (NdFeB) and two soft-magnetic (ferrite and pure Fe) helical microrobots. All designs exhibited similar linear behavior up to their step-out frequency, with the hard-magnetic helix achieving a step-out frequency and maximum speed 4.5 times higher compared to the soft-magnetic designs.

The tapered helix achieved the highest step-out frequency among all soft-magnetic designs, but also had the lowest propulsion efficiency (slope: (0.57(1)), as can be seen in Fig. 4. This enhancement in speed and step-out frequency is attributed to the reduced width and increased spacing between the microrobot and surrounding surfaces, which decreases rotational friction. Although this design slightly compromises propulsion efficiency, the threefold increase in maximum speed outweighs this reduction. It should be noted that the step-out frequency of hard-magnetic tapered helices exceeded the experimental limit of 5 Hz, preventing direct confirmation of the three-fold increase in step-out frequency and maximum speed. Reducing the magnetic field strength could lower the step-out frequency to within the experimental limit of 5 Hz. However, this would also narrow the operational frequency range of the soft-magnetic microrobots, reducing result accuracy. Therefore, this approach was not pursued. Given the identical slopes and torque-dependent propulsion behavior observed in the regular helical designs, however, it is likely that a similar threefold increase applies to the hard-magnetic tapered helical designs. Furthermore, the higher rotational speeds of this design may also improve the physical ablation of structures with shear-thinning properties, such as biofilms [23]. However, further research is needed to quantify this effect.

Fig. 5 shows that the tapered ribbon achieved the highest maximum speed among all tested designs, which could shorten procedure times in biomedical applications. Its step-out frequency was twice that of the

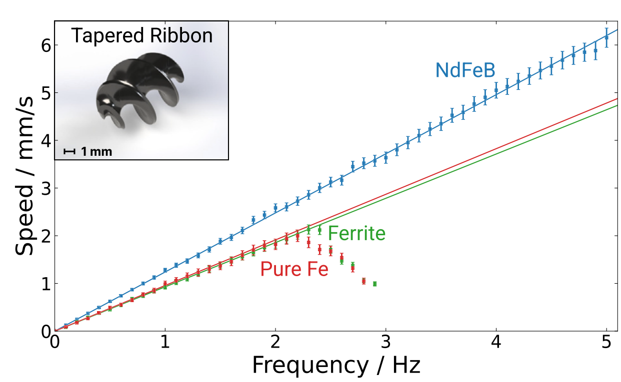

Fig. 5. Measured translation speed as a function of external magnetic field rotation frequency for one hard-magnetic (NdFeB) and two soft-magnetic (ferrite and pure Fe) ribbon-shaped microrobots. This design achieved the highest maximum speeds among all designs.

regular helix, while its maximum speed was 3.5 times greater. Despite having a step-out frequency lower than the tapered helix, the tapered ribbon achieved the highest maximum speed. This underscores the intricate relationship between rotational resistance and propulsion. The larger surface area of the ribbon-shaped design may also allow for greater drug loading and faster release. Interestingly, a small but statistically significant efficiency gap was observed between hard- and soft-magnetic ribbon-shaped designs, with slopes of 1.24(2) and 0.95(2) respectively. This likely occurred because the thinner ribbon walls made the transverse rods in the soft-magnetic designs contribute more to drag. In contrast, the thicker overall structure of the helical designs resulted in minimal additional drag from the transverse rod. Nevertheless, the ribbon-shaped designs achieved the highest maximum speed of all tested microrobots.

The microrobots used in our experiments are roughly twenty times larger than the dimensions envisioned for medical applications. Although the flow physics at low Reynolds number remains identical when scaling down, other forces change their relative importance. Because mass scales with volume while viscous drag scales only with the characteristic length, gravitational effects become much less dominant as robots are miniaturised. As a result, sub-millimeter robots will sediment more slowly and suffer less from hydrodynamic wall effects. However, once such small robots make contact with a wall, adhesive surface forces (electrostatic, double-layer, and van der Waals) become dominant and can lead to undesired sticking. Sticking may be suppressed by suitable surface engineering, such as applying biocompatible coatings to reduce charge interactions or hydrophobic adhesion.

5. Conclusions

We compared the propulsion under Stokes-flow of helical microrobots of 10 mm length actuated by an external rotating magnetic field, using either hard- or soft-magnetic elements and three representative shapes. This allowed us to isolate the effects of magnetic material and geometry on the maximum propulsion speed.

Helical microrobots incorporating hard-magnetic materials outperform their soft-magnetic counterparts under rotating magnetic fields, achieving a 4.5-fold higher step-out frequency and corresponding maximum propulsion speed under matched magnetic volume, field strength, and viscosity at low Reynolds numbers. Notably, for soft-magnetic materials, the generated torque is independent of magnetic susceptibility, resulting in identical propulsion characteristics for comparable geometric designs for external magnetic field strengths below the saturation value of approximately 23 mT for ferrite and 86 mT for pure Fe. Furthermore, employing a tapered ribbon-shaped design was shown to improve maximum propulsion speed by a factor of 3.5 compared to a regular helical design, underscoring the influence of geometry on microrobot performance.

These results demonstrate that replacing permanent-magnet alloys with bio-compatible soft-magnetic iron cores still allows for effective propulsion while improving biocompatibility. The observed performance differences provide a quantitative basis for informed material and design selection. This enables designers to balance the propulsion advantages of hard magnets against the biocompatibility of soft-magnetic alternatives. It also allows them to select the most suitable geometric design for their application.

This work was limited to propulsion along a line. Future work should explore navigation in more dimensions, in confined environments with obstacles [24–26]. Since many microrobots will be used, interaction needs to be addressed [27]. Next to navigation, one should consider microrobot functionalities beyond propulsion, with a particular focus on heating efficiency for thermal ablation and controlled drug release [28]. Comparing hard- and soft-magnetic materials in this context would offer a more comprehensive understanding of their respective advantages and limitations, ultimately guiding the design and application of microrobots for specific clinical tasks.

CRediT authorship contribution statement

Joost Wijnmaalen: Writing – review & editing, Writing – original draft, Visualization, Validation, Software, Methodology, Investigation, Formal analysis, Data curation, Conceptualization. **Leon Abelmann:** Writing – review & editing, Supervision, Methodology, Investigation, Formal analysis, Conceptualization. **Iulian Apachitei:** Writing – review & editing, Validation, Supervision, Project administration, Methodology, Funding acquisition, Conceptualization.

Declaration of competing interest

The authors declare that they have no known competing financial interests or personal relationships that could have appeared to influence the work reported in this paper.

Acknowledgments

During the preparation of this work the author(s) used ChatGPT in order to correct errors in spelling and grammar, and to improve style. The authors reviewed and edited the content as needed and take full responsibility for the content of the published article.

Appendix A. Magnetic field validation

Fig. 6 shows that the variation in measured magnetic field is limited to 1.5% over the actuation region.

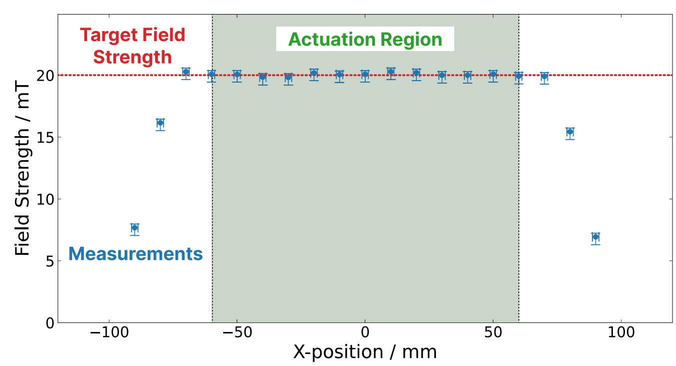

Fig. 6. Measured magnetic field strength along the central axis of the rotating magnetic field setup (x-axis). A 20 mT field was maintained across the 120 mm wide actuation region, with little deviation from the target field.

Appendix B. Supplementary data

Supplementary data to this article can be found online at doi:10.1016/j.sna.2026.117463.

Data availability

Data will be made available on request.

References

[1] M.C.J. de Boer, L.-J.W. Ligtenberg, I. Mulder, C. Goulas, Wireless mechanical and hybrid thrombus fragmentation of ex vivo endovascular thrombosis model in the iliac artery, Appl. Phys. Rev. 12 (2025) 011416, https://doi.org/10.1063/5.0233677

[2] H.H. Tran, A. Watkins, M.J. Oh, A. Babeer, T.P. Schaer, E. Steager, H. Koo, Targeting biofilm infections in humans using small scale Robotics, Trends Biotechnol. 42 (2) (2023) 479–495, https://doi.org/10.1016/j.tibtech.2023.10.004

[3] H. Ceylan, I.C. Yasa, O. Yasa, A.F. Tabak, J. Giltinan, M. Sitti, 3D-printed biodegradable microswimmer for theranostic cargo delivery and release, ACS Nano 13 (2019) 3353, https://doi.org/10.1021/acsnano.8b09233

[4] C. Chen, L. Chen, Y. Yi, C. Chen, L.-F. Wu, T. Song, Killing of staphylococcus aureus via magnetic hyperthermia mediated by magnetotactic bacteria, Appl. Environ. Microbiol. 82 (2016) 2219, https://doi.org/10.1128/AEM.04103-15

[5] J. Li, M. Pumera, 3D printing of functional microrobots, Chem. Soc. Rev. 50 (2021) 2794, https://doi.org/10.1039/D0CS01062F

[6] S. Ebbens, J. Howse, In pursuit of propulsion at the nanoscale, Soft Matter 6 (2010) 726, https://doi.org/10.1039/b918598d
[7] I.M. Longman, A.M. Lavie, On the swimming of a “pod”, IMA J. Appl. Math. 2 (1966) 273, https://doi.org/10.1093/imamat/2.3.273
[8] S. Mohanty, J. Zhang, J.M. McNeill, T. Kuenen, F.P. Linde, J. Rouwkema, S. Misra, Acoustically-actuated bubble-powered rotational micro-propellers, Sens. Actuators B Chem. 347 (2021) 130589, https://doi.org/10.1016/j.snb.2021.130589
[9] B. Nelson, J. Abbott, K. Peyer, M. Cosentino, L. Zhang, L. Dong, I. Kaliakatsos, How should microrobots swim? Int. J. Robot. Res. 28 (2009) 1434, https://doi.org/10.1177/0278364909341658
[10] M. Sitti, D.S. Wiersma, Pros and cons: magnetic versus optical microrobots, Adv. Mater. 32 (2020) e1906766, https://doi.org/10.1002/adma.201906766
[11] Z. Ren, W. Hu, X. Dong, M. Sitti, Multi-functional soft-bodied jellyfish-like swimming, Nat. Commun. 10 (2019) 2703, https://doi.org/10.1038/s41467-019-10549-7
[12] W. Hu, G.Z. Lum, M. Mastrangeli, M. Sitti, Small-scale soft-bodied robot with multimodal locomotion, Nature 554 (2018) 81, https://doi.org/10.1038/nature25443
[13] V.E. Donohue, F. McDonald, R. Evans, In vitro cytotoxicity testing of neodymium-iron-boron magnets, J. Appl. Biomater. 6 (1995) 69, https://doi.org/10.1002/jab.770060110
[14] M. Suter, L. Zhang, E.C. Siringil, C. Peters, T. Luehmann, O. Ergeneman, K.E. Peyer, B.J. Nelson, C. Hierold, Superparamagnetic microrobots: fabrication by two-photon polymerization and biocompatibility, Biomed. Microdevices 15 (2013) 997, https://doi.org/10.1007/s10544-013-9791-7
[15] M. Sitti, H. Ceylan, W. Hu, J. Giltinan, M. Turan, S. Yim, E. Diller, Biomedical applications of untethered mobile milli/microrobots, in: Proceedings of the IEEE, vol. 103, 2015, pp. 205, https://doi.org/10.1109/JPROC.2014.2385105
[16] E.P. Furlani, Phpermanent magnet and electromechanical devices, In E.P. Furlani (Ed.), Electromagnetism, Academic Press, San Diego, 2001, pp. 97–205, https://doi.org/10.1016/B978-012269951-1/50004-8
[17] J.J. Abbott, O. Ergeneman, M.P. Kummer, A.M. Hirt, B.J. Nelson, Modeling magnetic torque and force for controlled manipulation of soft-magnetic bodies, IEEE Trans. Robot. 23 (2007) 1247, https://doi.org/10.1109/TRO.2007.910775
[18] J.A. Osborn, Demagnetizing factors of the general ellipsoid, Phys. Rev. 67 (351) (1945), https://doi.org/10.1103/PhysRev.67.351
[19] X. Wang, C. Hu, S. Pané, B.J. Nelson, Dynamic modeling of magnetic helical microrobots, in: IEEE Robotics and Automation Letters, vol. 7, 2022, pp. 1682, https://doi.org/10.1109/LRA.2020.3049112
[20] D.P. Kingma, J. Ba, Adam: A Method for Stochastic Optimization, arXiv:1412.6980, 2017, https://doi.org/10.48550/arXiv.1412.6980
[21] Y.P. Klein, L. Abelmann, J.G.E. Gardeniers, Influence of the distribution of the properties of permanent magnets on the field homogeneity of magnet assemblies for mobile NMR, IEEE Trans. Magn. 57 (1) (2021), https://doi.org/10.1109/tmag.2021.3077301
[22] J. Lin, Z. Zhu, X. Jing, M. Lu, Y. Gu, Magnetic driven double curved conical microhelical robot, Adv. Theory Simul. 4 (2021) 2100189, https://doi.org/10.1002/adts.202100189
[23] L. Prades, S. Fabbri, A.D. Dorado, X. Gamisans, P. Stoodley, C. Picioreanu, Computational and experimental investigation of biofilm disruption dynamics induced by high-velocity gas jet impingement, mBio 11 (2020), https://doi.org/10.1128/mbio.02813
[24] S. Zhong, Y. Hou, Q. Shi, Y. Li, H.-W. Huang, Q. Huang, T. Fukuda, H. Wang, Spatial constraint-based navigation and emergency replanning adaptive control for magnetic helical microrobots in dynamic environments, IEEE Trans. Autom. Sci. Eng. 21 (2024) 7180, https://doi.org/10.1109/tase.2023.3339637
[25] S. Zhong, S. Guo, T. Sun, H.-W. Huang, Q. Shi, Q. Huang, T. Fukuda, H. Wang, Paired interactions of magnetic millirobots in confined spaces through data-driven disturbance rejection control under global input, in: IEEE/ASME Transactions on Mechatronics, vol. 1, 2025, https://doi.org/10.1109/tmech.2024.3521085
[26] Z. Xin, S. Zhong, A. Wu, Z. Zheng, Q. Shi, Q. Huang, T. Fukuda, H. Wang, Dynamic control of multimodal motion for bistable soft millirobots in complex environments, IEEE Trans. Robot. 41 (2025) 2662, https://doi.org/10.1109/tro.2025.3551541
[27] Y. Feng, J. Zhao, Z. Zhao, K. Chen, P. Li, J. Cong, L. Pan, M. Liu, Y. Liu, Precision engineering of nanorobots: toward single atom decoration and defect control for enhanced microplastic capture, Appl. Phys. Express 16 (2023) 067001, https://doi.org/10.35848/1882-0786/acd679
[28] W. Yang, X. Wang, Z. Ge, H. Yu, Magnetically controlled millipede inspired soft robot for releasing drugs on target area in stomach, in: IEEE Robotics and Automation Letters, vol. 9, 2024, pp. 3846, https://doi.org/10.1109/lra.2024.3372467